Persistent Climate Model Biases in the Atlantic Ocean's Freshwater Transport

René M. van Westen[1] and Henk A. Dijkstra[1]

[1]Institute for Marine and Atmospheric research Utrecht, Department of Physics, Utrecht University, Utrecht, the Netherlands

Correspondence: René M. van Westen <r.m.vanwesten@uu.nl>

Abstract. The Atlantic Meridional Overturning Circulation (AMOC) is considered to be one of the most dangerous climate tipping elements. The salt-advection feedback plays an important role in AMOC tipping behaviour and its strength is strongly connected to the freshwater transport carried by the AMOC at 34°S, below indicated by F_{ovS}. Available observations have indicated that F_{ovS} has a negative sign for the present-day AMOC. However, most climate models of the Coupled Model Intercomparison Project (CMIP, phase 3 and phase 5) have an incorrect F_{ovS} sign. Here, we analyse a high-resolution and a low-resolution version of the Community Earth System Model (CESM) to identify the origin of these F_{ovS} biases. Both CESM versions are initialised from an observed ocean state and F_{ovS} biases quickly develop under fixed pre-industrial forcing conditions. The most important model bias is a too fresh Atlantic Surface Water, which arises from deficiencies in the surface freshwater flux over the Indian Ocean. The second largest bias is a too saline North Atlantic Deep Water and arises through deficiencies in the freshwater flux over the Atlantic Subpolar Gyre region. Climate change scenarios branched from the pre-industrial simulations have an incorrect F_{ovS} upon initialisation. Most CMIP phase 6 models have similar biases as in the CESM. Due to the biases, the value of F_{ovS} is not in agreement with available observations and the strength of the salt advection feedback is underestimated. Values of F_{ovS} are projected to decrease under climate change and their response are also dependent on the various model biases. To better project future AMOC behaviour, an urgent effort is needed to reduce biases in the atmospheric components of current climate models.

1 Introduction

The Atlantic Meridional Overturning Circulation (AMOC) plays an important role in global climate because of its meridional transport of heat and salt. The present-day AMOC has a strength of 16 – 19 Sv (1 Sv = 10^6 m s^{-1}) near 26°N (Smeed et al., 2018) and effectively transports heat northwards, with a value of 1.5 PW at 26°N (Johns et al., 2011). The AMOC is considered to be one of the most important tipping elements (Armstrong McKay et al., 2022) and could, under future climate change, collapse to a state with a much weaker strength and corresponding weaker heat transport (Mecking and Drijfhout, 2023). It is a dangerous tipping element because, due to an AMOC collapse, large changes in sea surface temperatures, precipitation patterns, sea level and tropical cyclones (McFarlane and Frierson, 2017; Orihuela-Pinto et al., 2022; van Westen et al., 2023) can occur within a few decades.

Although reconstructed time series of the AMOC strength over the historical record appear to indicate a weakening of the AMOC (Caesar et al., 2021), the more recent direct observations indicate no decline in AMOC strength over the past 30 years (Worthington et al., 2021). Both time series of AMOC strength are relatively short and a longer observational record is required (Lobelle et al., 2020) to settle this debate. The idea of an AMOC collapse originates from conceptual models (Stommel, 1961; Castellana et al., 2019) and such collapses have been found in Earth System Models of Intermediate Complexity (Rahmstorf et al., 2005; Den Toom et al., 2012). The transitions in these models are related to the existence of a multi-stable AMOC regime where different equilibrium states exist under the same (freshwater) forcing conditions. The stability and transitions to the collapsed state are affected by the salt-advection feedback (Marotzke, 2000; Peltier and Vettoretti, 2014), a positive feedback in which salinity anomalies are amplified through their effect on the AMOC strength and pattern.

As a measure of the salt-advection feedback strength, an indicator was developed (Rahmstorf, 1996; de Vries and Weber, 2005) based on F_{ovS} (Weijer et al., 2019), the net Atlantic freshwater transport by the AMOC at 34°S (the southern boundary of the Atlantic Ocean). When $F_{ovS} < 0$ (> 0), the AMOC transports net saline (fresh) water w.r.t. 35 g kg^{-1} into the Atlantic Ocean and the salt-advection feedback is positive (negative). Present-day hydrographic observations show negative values of $F_{ovS} < 0$ (Bryden et al., 2011; Garzoli et al., 2013) and also a recent Lagrangian study of reanalysis data shows the same property (Rousselet et al., 2021). Clearly, most models used in the Coupled Model Intercomparison Projects (CMIP) phase 3 (CMIP3) (Drijfhout et al., 2011) and phase 5 (CMIP5) (Mecking et al., 2017) have $F_{ovS} > 0$ and hence do not adequately capture the salt-advection feedback.

AMOC responses under surface freshwater forcing or climate change are substantially different when comparing climate models with a different F_{ovS} sign (Jackson, 2013; Liu et al., 2017), in particular for models with a positive F_{ovS} bias. Freshwater flux adjustments shift the F_{ovS} to its correct regime and then substantially influence AMOC responses under varying forcing conditions (Jackson, 2013; Liu et al., 2017). It is then possible to find an AMOC collapse in these models (Yin and Stouffer, 2007; Liu and Wang, 2014; Mecking et al., 2016). In conceptual models, the value of F_{ovS} is directly related to the strength of the salt-advection feedback. This feedback plays a crucial role in AMOC weakening and when it is not well represented the AMOC response is likely to be underestimated. Some studies (Dijkstra, 2007; Huisman et al., 2010) suggest a more versatile role for F_{ovS} in which the sign of F_{ovS} is also an indicator of whether the AMOC is in a multi-stable regime or not. This then would imply that most models in CMIP3 and CMIP5 underrepresent AMOC tipping as they have positive F_{ovS} biases (Drijfhout et al., 2011; Mecking et al., 2017). These biases could also persist in the latest CMIP phase 6 (CMIP6). A first analysis on CMIP6 suggests no clear relation between F_{ovS} sign and AMOC responses (Jackson et al., 2022), but it comprises only 8 CMIP6 models

To understand the response of CMIP6 models to climate change scenarios, it is important to determine their biases in F_{ovS}. Here, we perform this analysis in 39 CMIP6 models and a high-resolution (HR) and low-resolution (LR) version of the Community Earth System Model (CESM). The main aim of the paper is to identify the origin of these F_{ovS} biases, which is important for determining how such biases can be corrected. In section 2 a brief description of the HR-CESM, LR-CESM and CMIP6 models is provided, together with a description of the freshwater transport analysis. In section 3, we systematically analyse the origin of the F_{ovS} biases in the HR-CESM and LR-CESM models and provide a comparison with the origin of

60   the biases in the CMIP6 models. A summary and discussion of the results with the main conclusions are given in the final section 4.

2   Climate Model Simulations and Methods

We analysed results from the 500-year long pre-industrial (PI) control simulations for the HR-CESM and LR-CESM as provided by Chang et al. (2020). The LR-CESM has a horizontal resolution of $1°$ for both the ocean and atmosphere components,

65   while the HR-CESM has a strongly eddying ocean ($0.1°$ horizontal resolution) and resolves tropical cyclones in the atmospheric component ($0.25°$ horizontal resolution). The ocean components in the HR-CESM and LR-CESM have the same 60 non-equidistant vertical layers down to 5,375 m, with the highest vertical resolution near the surface (10 m) and lowest resolution near the bottom (250 m). The HR-CESM has two additional vertical layers below 5,375 m but their effect is very limited as only a few grid cells extend below 5,375 m. Increasing the horizontal ocean resolution to $0.1°$ strongly improves

70   the global ocean circulation and reduces ocean-related biases (Small et al., 2014; Jüling et al., 2021; van Westen et al., 2020; van Westen and Dijkstra, 2021). The ocean component was initialised with the January-mean climatologies (from the World Ocean Atlas) for potential temperature and salinity and from rest (Chang et al., 2020). At model year 250 of the PI control simulation, another simulation was branched off which is forced by historical observations (1850 – 2005) and then followed by the RCP8.5 climate change forcing scenario (2006 – 2100), which we refer to as the Hist/RCP8.5 simulation.

75   For comparison with the Hist/RCP8.5 (1994 – 2020) CESM simulations, we used the eddy-resolving ($1/12°$) Copernicus Marine global reanalysis product (1994 – 2020) as 'observations'. For the CMIP6 models we retained the historical (1994 – 2014) followed by SSP5-8.5 (2015 – 2100) forcing scenario, which we refer to as the Hist/SSP5-8.5 simulation. Note that the forcing scenarios are different between the CESM (Hist/RCP8.5) and CMIP6 scenarios (Hist/SSP5-8.5), but the projected temperature in 2100 are both high-end scenarios ($+3°C$ – $+5°C$ w.r.t. the pre-industrial period). The monthly-averaged model

80   output from the CESM, reanalysis and CMIP6 is converted to yearly-averaged fields. The analyses here are conducted on these yearly-averaged fields and on their native grid.

The freshwater transport by the overturning component (F_{ovS}) and the azonal (gyre) component (F_{azS}) at $34°$S are determined as:

$$F_{\mathrm{ovS}} = F_{\mathrm{ov}}(y = 34°\mathrm{S}) = -\frac{1}{S_0} \int_{-H}^{0} \left[\int_{x_W}^{x_E} v^* \mathrm{d}x \right] [\langle S \rangle - S_0] \, \mathrm{d}z \tag{1a}$$

85
$$F_{\mathrm{azS}} = F_{\mathrm{az}}(y = 34°\mathrm{S}) = -\frac{1}{S_0} \int_{-H}^{0} \int_{x_W}^{x_E} v' S' \mathrm{d}z \tag{1b}$$

where $S_0 = 35$ g kg^{-1} is a reference salinity. The v^* is defined as $v^* = v - \hat{v}$, where v is the meridional velocity and $\hat{v}$ the (full depth) section spatially-averaged meridional velocity. In addition, $\langle S \rangle$ indicates the zonally-averaged salinity and primed quantities (v' and S') are deviations from their respective zonal means (Jüling et al., 2021).

The F_{ovS} can be separated into a contribution of four different water masses, i.e., the Atlantic Surface Water (ASW), the Antarctic Intermediate Water (AAIW), the North Atlantic Deep Water (NADW) and the Antarctic Bottom Water (AABW). The contribution for each water mass is determined similarly as in (1a), but only vertically integrating between the boundaries of each water mass. The boundaries for the ASW, AAIW and NADW and AABW are determined by first locating the NADW layer. This layer has negative v^* and is found around $1{,}000 - 4{,}000$ m depths. Directly above the NADW, where v^* becomes positive, we define the AAIW. The AAIW is bounded above by the 500 m depth level and the ASW is defined between the 500 m depth level and the surface. The AABW is located directly below the NADW, where v^* becomes positive, and extends down to the bottom. The layer thickness of each of these water masses may vary over time due to changes in the meridional velocity profile. We did not define the water masses based on their T, S-related properties as climate change alters these properties.

The AMOC strength is defined as the total meridional mass transport at $26°$N over the upper $1{,}000$ m:

$$\text{AMOC}(y = 26°\text{N}) = \int_{-1000}^{0} \int_{x_W}^{x_E} v \, \mathrm{d}x \mathrm{d}z \tag{2}$$

This AMOC strength may deviate from the maximum AMOC strength as the maximum varies around $1{,}000$ m depth, but using this metric is then consistent between all climate model simulations and reanalysis. All models provide the meridional velocity as standard output and a few models also provide the AMOC streamfunction. The AMOC strength is very consistent when determining this quantity by using either the meridional velocities or AMOC streamfunction (Menary et al., 2020). For consistency and to include as many CMIP6 models as possible we determined the AMOC strength as in (2).

The trends computed below are derived from a linear least-square fit to the yearly-averaged time series. The significance of each trend is determined following the procedure outlined in Santer et al. (2000), while taking into account the reduction of degrees of freedom for time series which are not statistically independent. Using the reduced degrees of freedom and the two-sided critical Student-t values, one can determine the significance of having a trend different from zero (the null hypothesis).

3 Results

3.1 The PI Control Simulations

In this section we focus on the PI control simulations to study the transient development of the freshwater biases at $34°$S. The values of F_{ovS} and F_{azS} for the PI control CESM simulations are shown in the Figures 1a,b,c,d with the PI control in black and the Hist/RCP8.5 simulation in red. The first 20 model years of the HR-CESM PI control are not available. From the initial observed ocean state it is striking that the value of F_{ovS} drifts from negative to positive values within the first 250 model years of the PI control simulations. The quantity F_{azS} remains fairly constant during most parts of the PI control simulations (model years $21 - 500$), but in the first 20 years there are substantial changes due to the changing salinity fields at $34°$S over the upper $1{,}000$ m and in particular over the upper 500 m (not shown). The salinity fields become less zonally coherent (w.r.t. initialisation) and induce the F_{azS} minimum in model year 7. Once the salinity fields (and velocity fields) are adjusted, F_{azS}

120 remains fairly constant for the remaining part of the PI control simulation in the LR-CESM. The HR-CESM displays more natural variability in F_{azS} than the LR-CESM.

The upper 500 m salinity fields at 34°S are (strongly) influenced by Agulhas Leakage and the water properties of the leakage have an Indian Ocean origin. The upper 100 m Indian Ocean strongly freshens by 0.3 g kg^{-1} in the first 10 years for the LR-CESM (Figure 1f). For the HR-CESM this is only 0.2 g kg^{-1} in the first 20 years (Figure 1e), where we used the initial value

125 of the LR-CESM for reference. The relatively large adjustment of the upper 100 m Indian Ocean salinities induce the temporal response in F_{azS} in the LR-CESM. It is possible that the HR-CESM shows a similar response but this can not be verified. The quantity F_{azS} reaches much faster an equilibrium state compared to the F_{ovS}. The AMOC also imports the relatively fresh water of Indian Ocean origin into the Atlantic basin and this contributes to the drift in F_{ovS}.

To better quantify the water mass contributions to F_{ovS} changes, we separate the total F_{ovS} over the four different water

130 masses and each contribution is shown in Figure 2. The F_{ovS} drift mainly originates from the ASW and the NADW water masses for both the HR-CESM and LR-CESM. The AAIW and AABW contributions show adjustments in the first 50 model years and then remain fairly constant over the remaining simulation period. The ASW contribution to the F_{ovS} drift is related to the strong freshening of the Indian Ocean. The upper Indian Ocean's freshening manifests itself within a decade, these are typical time scales of atmospheric adjustment while oceanic adjustments typically take much longer time. Indeed, there

135 is a strong precipitation response over the Indian Ocean which contributes to the freshening of the Indian Ocean, changes in evaporation are much smaller (not shown). These precipitation responses over the Indian Ocean are likely related to Intertropical Convergence Zone (ITCZ) biases (Mamalakis et al., 2021). The Indonesian Throughflow also imports more (net) fresh water into the Indian Ocean (not shown), but this can not solely explain the (strong) freshening of the Indian Ocean in the first decade of the LR-CESM. The negative salinity anomalies (w.r.t. initialisation) in the Indian Ocean eventually reach the

140 Agulhas Retroflection and through Agulhas Leakage affect the upper 500 m salinity fields at 34°S (i.e., the ASW). This leads to positive freshwater anomalies transported into the Atlantic Ocean which contribute to the F_{ovS} drift.

The NADW also contributes to the F_{ovS} drift (Figures 2e,f). The NADW is part of southward flowing limb of the AMOC and this water mass originates from deep water formation at the higher latitudes in the North Atlantic. This motion in this water mass is linked to the AMOC strength which is shown in Figures 3a,b. There is some adjustment in the first 100 model

145 years of the PI control simulations (AMOC is 0 Sv at initialisation), but thereafter it is in near equilibrium. The adjustment in AMOC strength during the first 100 years results in sea surface temperature (SST, insets in Figures 3a,b) responses. These SST responses induce surface salinity anomalies mainly through evaporation (not shown). These surface salinity anomalies undergo deep water transformation over the Labrador basin, Irminger basin or Iceland basin (i.e., regions of deep convection) and influence the salinities over these three basins at depth (1,000 – 3,000 m, Figures 3c,d).

150 The AMOC responses and related SST responses (Caesar et al., 2018) in the first 100 years are the opposite when comparing the HR-CESM and LR-CESM. The positive SST trends in the LR-CESM enhance evaporation and result in more saline surface waters at the higher latitudes compared to the HR-CESM. The surface salinities at the higher latitudes also increase in the HR-CESM (mainly over the East and West Greenland Current) but at a lower rate due to the reduced evaporation through lower SSTs. The different surface salinity changes are also reflected in the timing of the salinity maxima over the three deep
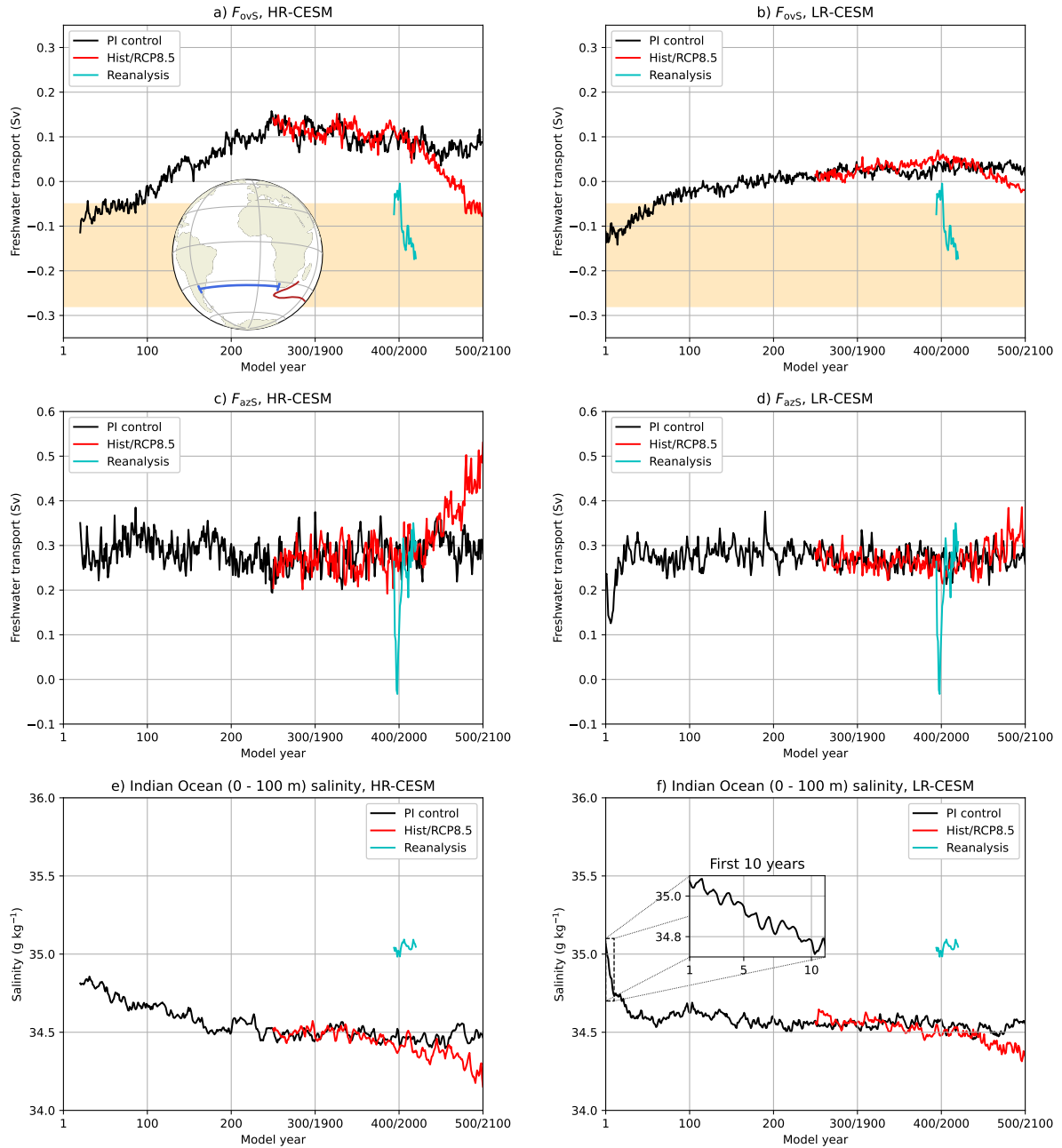
Figure 1. (a & b): The freshwater transport by the overturning component at $34°$S, F_{ovS}, for the a) HR-CESM and b) LR-CESM. The cyan-coloured curve shows reanalysis. The yellow shading indicates observed ranges (Garzoli et al., 2013; Mecking et al., 2017). The inset in panel a shows the region of interest, including the section at $34°$S (blue) and a schematic representation of the Agulhas Current and Retroflection (red). (c & d): Similar to panels a and b, but now for the azonal (gyre) component, F_{azS}. (e & f): The vertically-averaged (0 – 100 m) and spatially-averaged salinity over the Indian Ocean for the e) HR-CESM and f) LR-CESM, including reanalysis. The inset in panel f shows the volume-averaged salinity over the first 10 years (monthly averages).
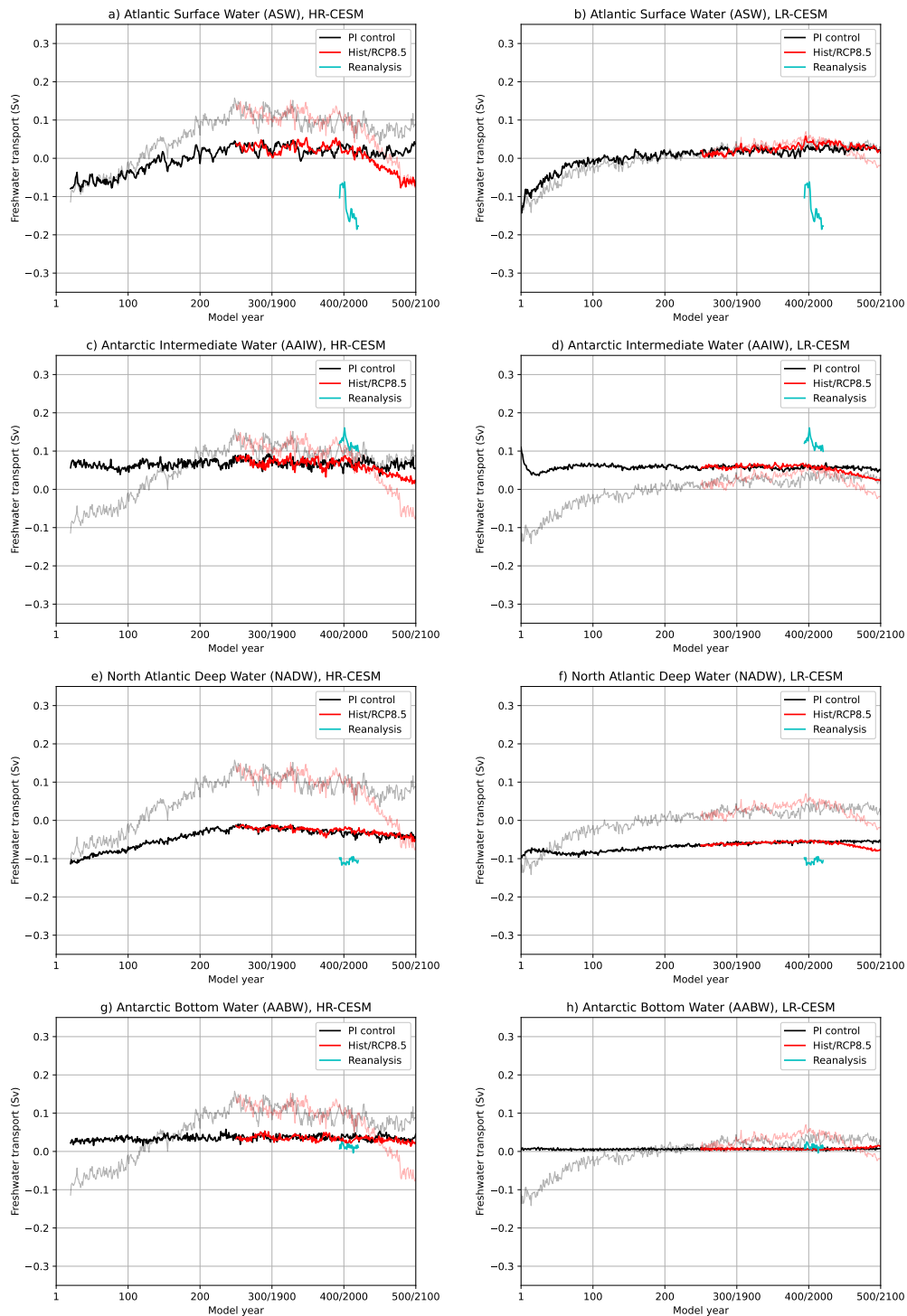
Figure 2. The F_{ovS} contributions for the four different water masses for the HR-CESM (left column) and LR-CESM (right column). The cyan-coloured curve shows reanalysis. The opaque curves show the freshwater transport by the overturning component, F_{ovS} (see also Figures 1a,b).
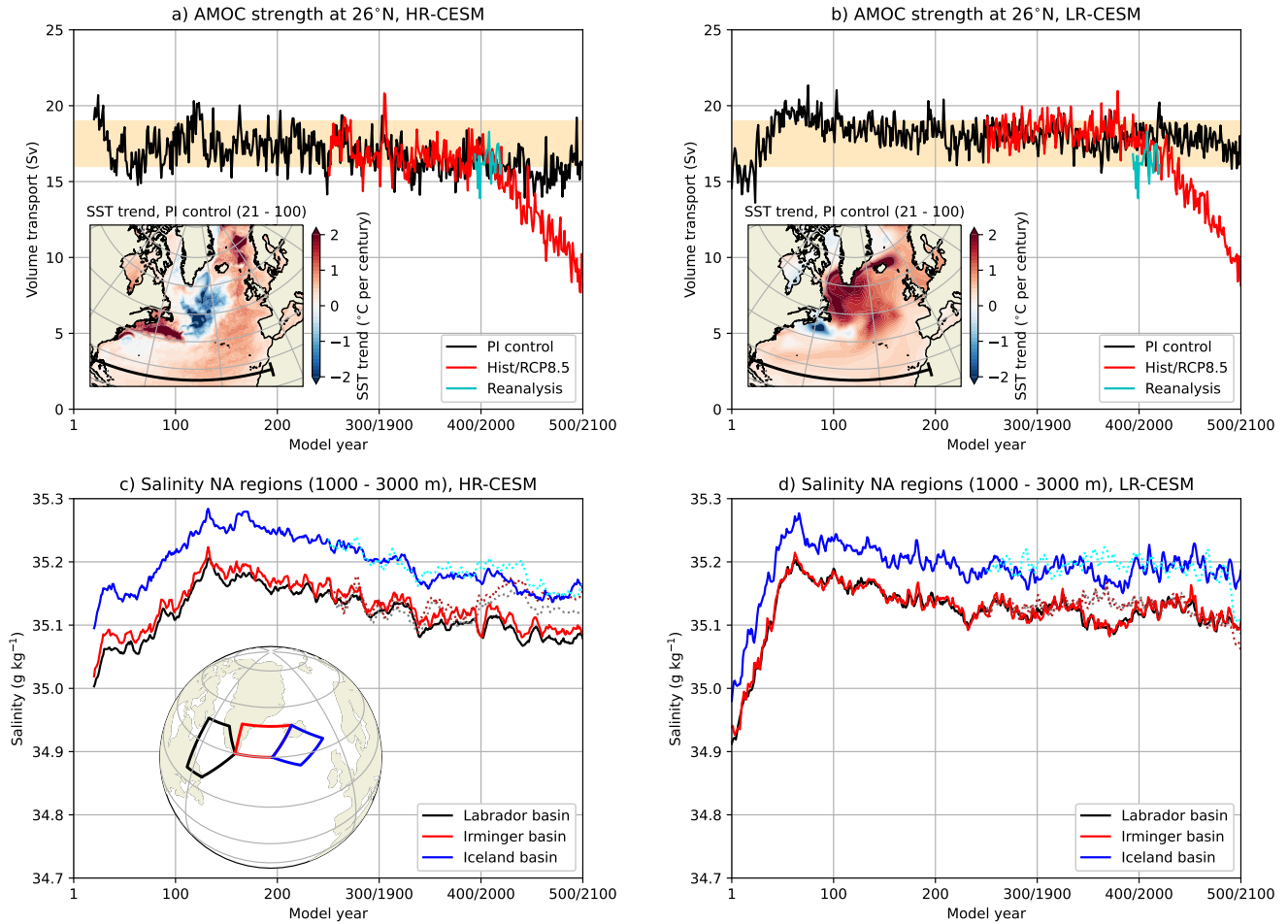
Figure 3. (a & b): The AMOC strength at 1,000 m and 26°N (determined at black section in inset) for the a) HR-CESM and b) LR-CESM. The cyan-coloured curve shows reanalysis. The yellow shading indicates observed ranges (Smeed et al., 2018; Worthington et al., 2021). Inset: The SST trend (PI control, model years 21 – 100). (c & d): The vertically-averaged (1,000 – 3,000 m) and spatially-averaged salinity over the Labrador basin, Irminger basin and Iceland basin (see inset in panel c) for the c) HR-CESM and d) LR-CESM. The solid (dotted) curves indicate the PI control (Hist/RCP8.5) simulation.

155   convection basins, which are around model year 65 for the LR-CESM and around model year 130 for the HR-CESM. The AMOC strength has a local maximum around the same years for the respective model. After the salinity maxima there is a gradual decrease in the salinity content over the three basins for both models, while the AMOC also declines by 0.5 Sv per century ($p < 0.01$, model years 130 – 500) for the HR-CESM and by 0.2 Sv per century ($p < 0.01$, model years 130 – 500) for the LR-CESM.

160   The newly-formed water mass in the three deep convection basins takes about 100 years to reach 34°S and then influence the NADW properties there. One expects a larger change in the NADW properties for the LR-CESM as the deep water formation

salinity responses are about twice as strong in the LR-CESM than in the HR-CESM (during the first 100 model years). Yet, the NADW contribution to F_{ovS} changes (Figures 2e,f) shows a stronger drift (model years $100 - 250$) in the HR-CESM (0.038 Sv per century, $p < 0.01$) than the LR-CESM (0.014 Sv per century, $p < 0.01$). The differences in the NADW freshwater transport trends are related to the ventilation rate of the NADW. By analysing the average water age of the NADW (not shown) we find that the NADW is ventilated faster in the HR-CESM than the LR-CESM. This larger ventilation rate is related to the high horizontal ocean model resolution in the HR-CESM resulting in much more eddy-induced horizontal mixing (w.r.t. the LR-CESM). After model year 250, the NADW freshwater transport slightly declines again (-0.011 Sv per century, $p < 0.01$) in the HR-CESM, which is consistent with the salinity maxima in the Labrador basin, Irminger basin and Iceland basin that are reached 100 years earlier. Over this later period, the LR-CESM shows a persistent positive NADW trend (0.004 Sv per century, $p < 0.01$) which contributes to the drift in F_{ovS}. This indicates that the salinity content of the deeper ocean in the LR-CESM takes a much longer time to adjust than the HR-CESM, in particular given that the salinity maxima of the Labrador basin, Irminger basin and Iceland basin are reached around model year 65 for the LR-CESM.

The Atlantic's northern boundary (at 60°N, F_{ovN}) also contributes to the freshwater budget of the Atlantic Ocean and the convergence/divergence of freshwater by the overturning circulation is indicated by $\Delta F_{ov} = F_{ovS} - F_{ovN}$ (Dijkstra, 2007; Weijer et al., 2019). For the HR-CESM PI control, F_{ovN} is about -0.03 Sv and its magnitude is smaller than F_{ovS} (Figure 4a), and hence $\Delta F_{ov} \approx F_{ovS}$. For the LR-CESM PI control, F_{ovN} contributes quite some more to ΔF_{ov} (Figure 4b). As a result, the values of ΔF_{ov} are fairly similar for the HR-CESM and LR-CESM between model years $200 - 500$.

3.2 The Present-day Comparison

In the previous subsection we analysed the onset of the F_{ovS} drift in the PI control simulations. Some quantities, such as the F_{azS} and the AAIW, showed some adjustments in the first 50 years, but those changes hardly contributed to the F_{ovS} drift. However, these quantities can have various biases when comparing this to present-day observations (i.e., reanalysis). To systematically compare the available reanalysis data ($1994 - 2020$) with the CESM, we analyse the same model years $1994 - 2020$ from the Hist/RCP8.5 simulations. The Hist/RCP8.5 simulations are indicated by the red-coloured curves and reanalysis by the cyan-coloured curves (Figures 1 through 3).

There are indeed large biases in the patterns of ASW, AAIW and NADW in the Hist/RCP8.5 simulations. Whereas the meridional velocities at 34°S are reasonably simulated (Figures 5a,b,c), the ASW is too fresh, in particular in the eastern part of the Atlantic (Figures 5d,e,f). The relatively fresh ASW is related to the surface salinities over the Indian Ocean which are too fresh (-0.5 g kg^{-1}) when comparing the Hist/RCP8.5 simulations with reanalysis (Figures 1e,f). On the other hand, the positive surface salinity anomalies in the North Atlantic, which undergo deep water transformation, result in a too salty NADW. The Hist/RCP8.5 simulations consequently have a positive F_{ovS} bias upon initialisation and during the years $1994 - 2020$. The F_{azS} and AMOC strength are reasonably simulated in both the HR-CESM and LR-CESM. The F_{azS} in reanalysis shows large variations before the year 2000 which is due to internal variability in the zonal salinity variations over the upper 500 m.

The AAIW originates from the Antarctic Convergence zone (near 50°S – 60°S) and submerges when flowing northward, as shown in Figure 6. In the HR-CESM, the shape (not the absolute values) and outcropping of the isopycnals resembles that
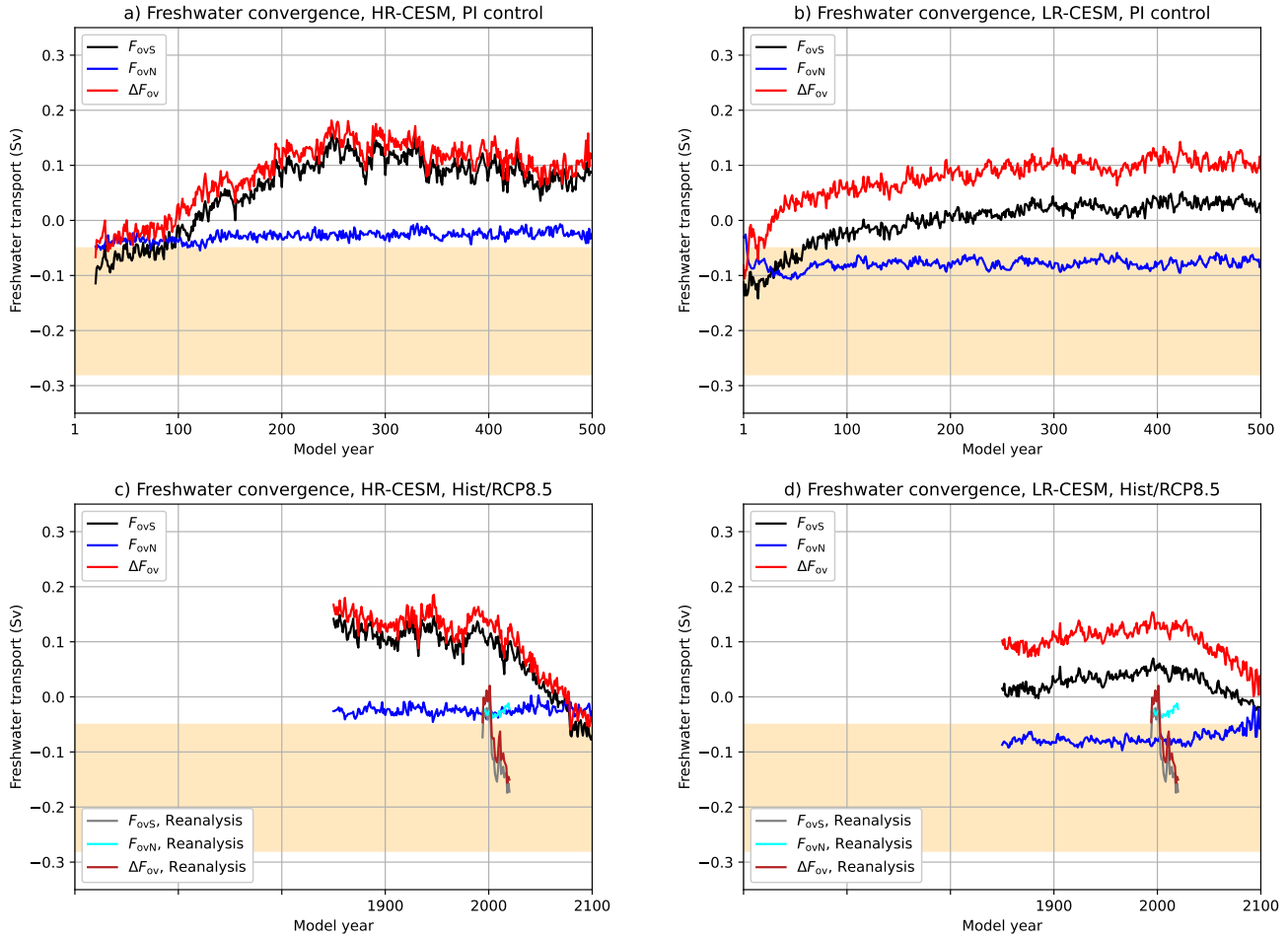
Figure 4. The freshwater transport by the overturning component at $34°S$ (black curve, F_{ovS}), $60°N$ (blue curve, F_{ovN}) and the freshwater convergence (red curve, $\Delta F_{\text{ov}} = F_{\text{ovS}} - F_{\text{ovN}}$) for the PI control (upper row) and Hist/RCP8.5 (lower row) simulations. The reanalysis is displayed in the lower row. The yellow shading indicates observed ranges for the F_{ovS}.
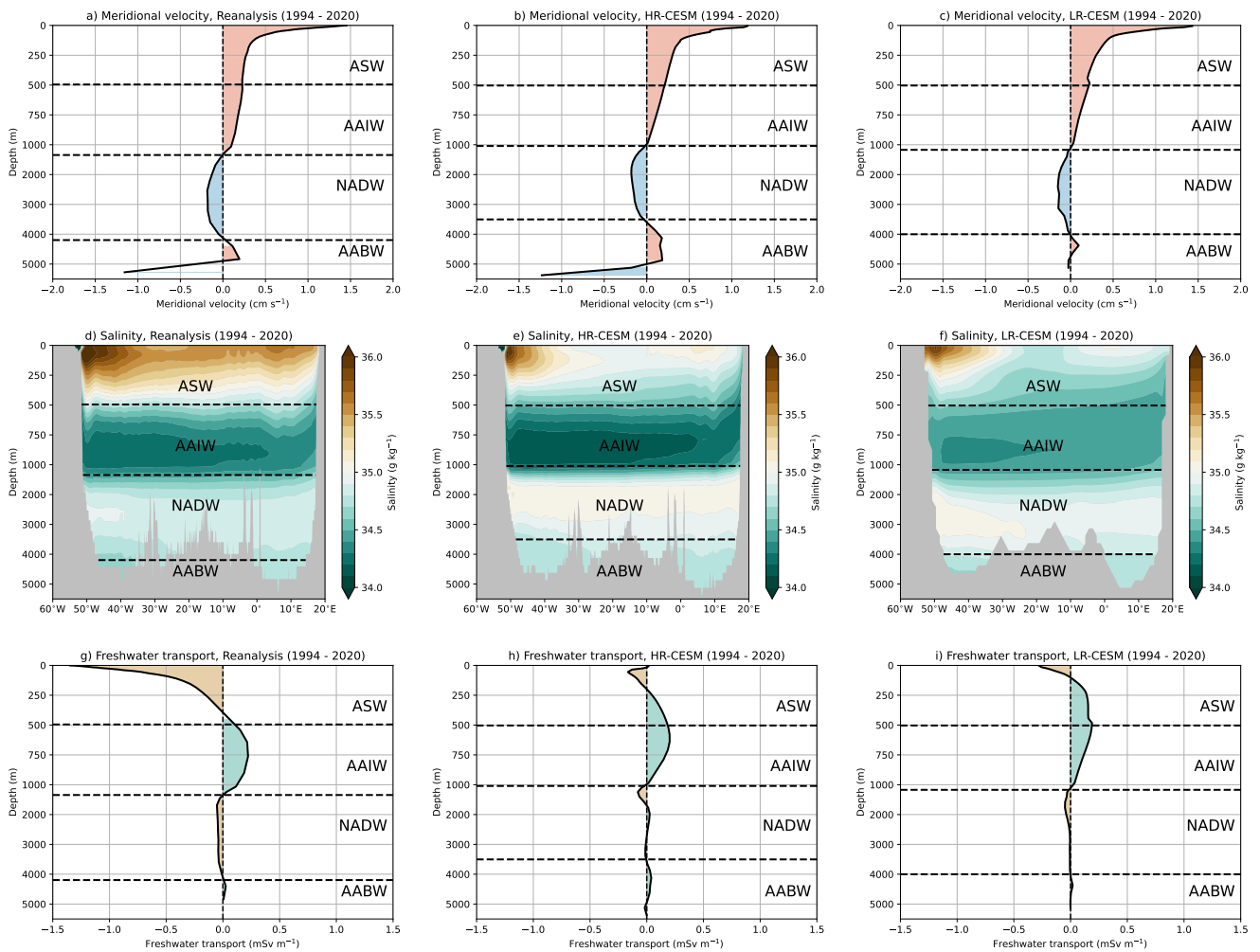
Figure 5. (Upper row): The present-day (1994 – 2020) zonally-averaged meridional velocity at 34°S. (Middle row): The present-day (1994 – 2020) salinity along 34°S. (Lower row): The present-day (1994 – 2020) freshwater transport with depth at 34°S. The present-day profiles originate from reanalysis, and the HR-CESM and LR-CESM under the Hist/RCP8.5 forcing scenario. Note that the vertical axis is cropped below 1,000 m depths.
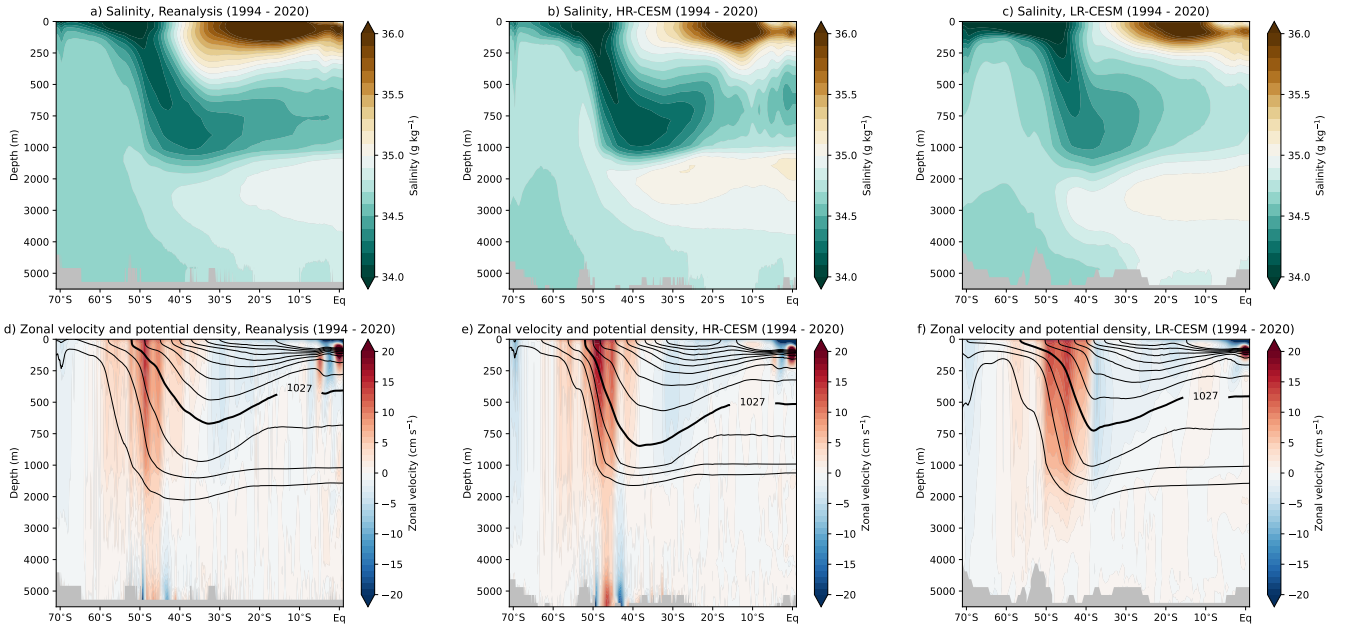
Figure 6. (Upper row): The present-day (1994 – 2020) and zonally-averaged (50°W – 20°E, Atlantic sector) salinity. (Lower row): The present-day (1994 – 2020) and zonally-averaged (50°W – 20°E, Atlantic sector) zonal velocity (shading) and potential density (contours are the isopycnals), the contours are each spaced by 0.25 kg m^{-3} and where the thick contour is the 1027 kg m^{-3} for reference. The present-day profiles originate from reanalysis, and the HR-CESM and LR-CESM under the Hist/RCP8.5 forcing scenario. Note that the vertical axis is cropped below 1,000 m depths.

of reanalysis and the pattern of the AAIW is well represented in the HR-CESM. The zonal velocities, which are related to the Antarctic Circumpolar Current (near 50°S), are slightly higher in the HR-CESM than in reanalysis. The shape and outcropping of the isopycnals are substantially different in the LR-CESM when comparing those to the reanalysis. The outcropping in the LR-CESM occurs further south giving rise to different water mass properties of the AAIW. The ventilation of the AAIW is

200 not that well resolved in the LR-CESM and this results in a relatively saline AAIW compared to reanalysis and HR-CESM (Figure 5). The relatively saline AAIW and the too weak meridional velocities (at 34°S) explain why the AAIW bias is larger in the LR-CESM than in the HR-CESM.

The biases in the three water masses ASW, NADW and AAIW result in freshwater transport biases at 34°S (Figures 5g,h,i), but the biases in the ASW and NADW are the most dominant and induce a positive F_{ovS} bias. The contribution of the AABW

205 is fairly small and hence we do not discuss it here. The value of F_{ovN} has a small contribution (-0.027 Sv, 1994 – 2020) to the freshwater convergence ΔF_{ov} in reanalysis. In the HR-CESM, the value of F_{ovN} (-0.030 Sv, 1994 – 2020) is close to reanalysis but for the LR-CESM (-0.080 Sv, 1994 – 2020) it is a factor 3 larger than in the reanalysis (Figure 4). This shows that $\Delta F_{\mathrm{ov}} \approx F_{\mathrm{ovS}}(34°\mathrm{S})$ in both the reanalysis and in the HR-CESM.

3.3 Climate Change Simulations

The present-day comparison between reanalysis and the CESM simulations shows biases in various oceanic quantities. There are also differences when comparing the HR-CESM and LR-CESM biases, which are likely related to the different horizontal resolutions between the two models. The oceanic responses under climate change are substantially different when analysing high-resolution and low-resolution climate models (van Westen et al., 2020; van Westen and Dijkstra, 2021) and such a response can also be expected for the freshwater transport at 34°S (Jüling et al., 2021). In this subsection we investigate the freshwater transport responses under the Hist/RCP8.5 scenario (model years 2000 – 2100).

The presented quantities in Figures 1 through 4 for the Hist/RCP8.5 simulations remain close to their PI control simulations under the historical forcing (1850 – 2005), but start to deviate in the last 100 years of the simulation. The values of F_{ovS} decrease under climate change (model years 2000 – 2100, Figures 1a,b) for both the HR-CESM (-0.19 Sv per century, $p < 0.01$) and LR-CESM (-0.076 Sv per century, $p < 0.01$). Changes in F_{ovS} can be induced by AMOC changes and/or by salinity changes. The AMOC weakens over the entire Atlantic Ocean and reduces the zonally-averaged meridional velocity magnitudes in the northward flowing branch (upper 1,000 m) and southward flowing branch (1,500 – 4,000 m); as shown in the insets in Figures 7e,f at 34°S. The AMOC strength (Figures 3a,b) decreases by -8.2 Sv per century ($p < 0.01$) and -8.9 Sv per century ($p < 0.01$) for the HR-CESM and LR-CESM simulations, respectively.

The vertically-averaged (0 – 100 m) salinity in the Atlantic Ocean increases under climate change, which is related to negative P-E trends (induced by higher evaporation rates through higher SSTs) over the Atlantic (Figures 7a,b,c,d). Changes in the South American Monsoon result in more precipitation over the South Atlantic Ocean (near 30°S). These changes are the strongest in the LR-CESM leading to a surface freshening around 30°S and 30°W. The upper 100 m salinity over the Indian Ocean decreases by about $0.17\,\mathrm{g\,kg^{-1}}$ per century ($p < 0.05$) for both the HR-CESM and LR-CESM, but there is a south-north dipole pattern in both salinity and P-E trends. The northward ITCZ shift over the Indian Ocean leads to a different precipitation pattern and results in positive salinity trends in the southern part of the Indian Ocean and, from this, in the Agulhas Leakage (Figures 7e,f). The azonal (gyre) component F_{azS} increases under climate change (Figures 1c,d) and these changes are mainly induced by altering the zonal salinity gradient along the 34°S section, in particular near the surface (0 – 250 m depths). In both the HR-CESM and LR-CESM this near-surface salinity gradient increases under climate (compare the salinity trends between the western and eastern part of the section) and this is most pronounced in the HR-CESM. The relatively saline water in the western part of the section is advected out of the Atlantic (via the Brazil Current) resulting in an F_{azS} increase. The F_{azS} trends are 0.21 Sv per century ($p < 0.01$) and 0.09 Sv per century ($p < 0.01$) for the HR-CESM and LR-CESM, respectively.

The salinity response at intermediate depths (250 – 1,000 m) at 34°S is the opposite for the HR-CESM and LR-CESM (Figures 7e,f) simulations. As discussed in the previous subsection, the outcropping of the isopycnals is different between the HR-CESM and LR-CESM and the outcropping latitude occurs further south in the LR-CESM (somewhere in the center of the Weddell Gyre). Changes in the surface water properties near the Weddell Gyre are therefore connected to the AAIW changes in the LR-CESM. The surface salinity trends over Weddell gyre are mainly negative (i.e., freshening) in the LR-CESM, whereas there are both positive and negative salinity trends in the HR-CESM. The primarily negative salinity trends in the LR-CESM
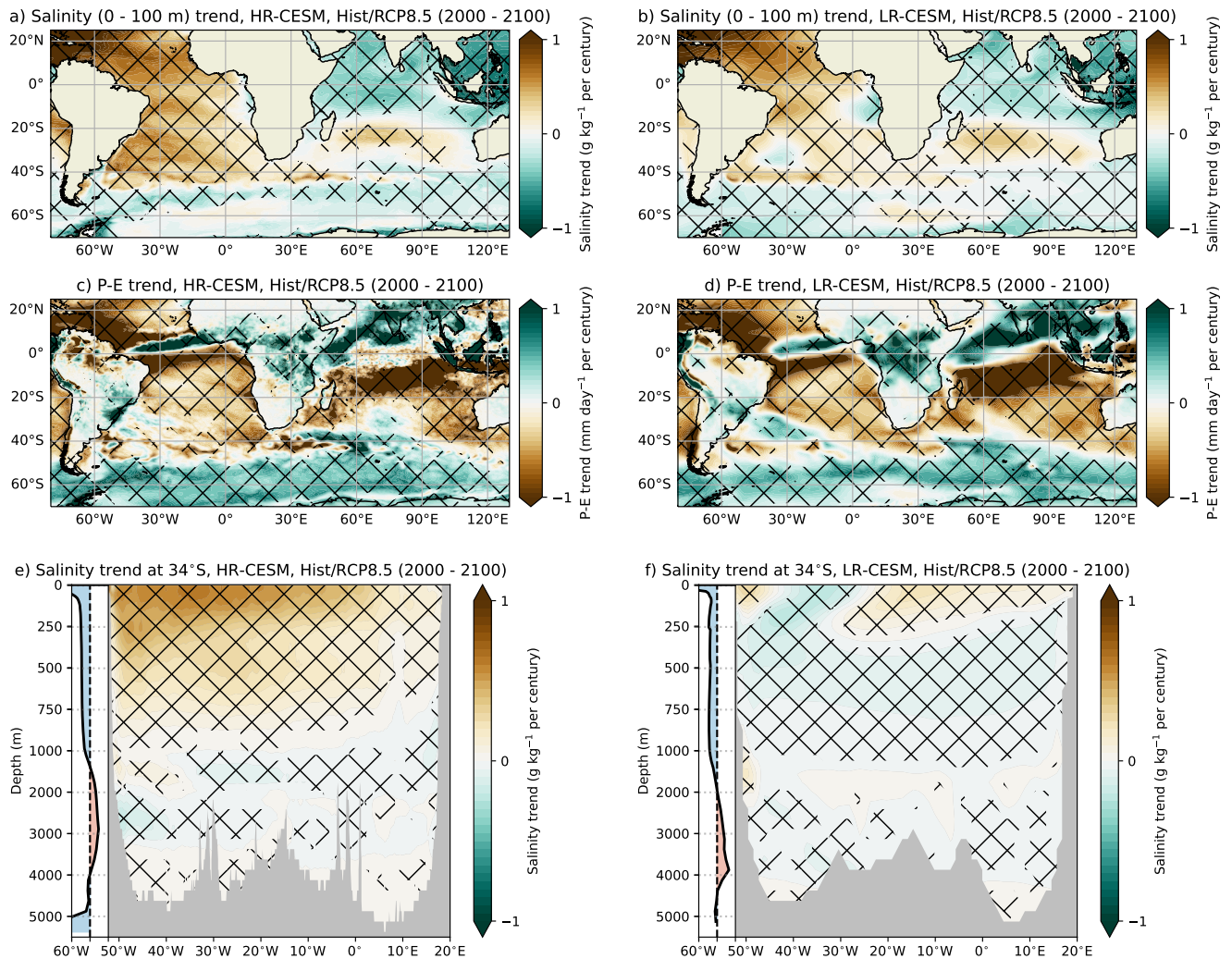
Figure 7. (a & b): The vertically-averaged (0 – 100 m) salinity trends (Hist/RCP8.5, model years 2000 – 2100) for the a) HR-CESM and b) LR-CESM. (c & d): The P-E trends (Hist/RCP8.5, model years 2000 – 2100) for the c) HR-CESM and d) LR-CESM. (e & f): The salinity trends (Hist/RCP8.5, model years 2000 – 2100) along 34°S for the e) HR-CESM and f) LR-CESM. Inset: The zonally-averaged meridional velocity trend at 34°S, the horizontal ranges are between -0.2 and 0.2 cm s^{-1} per century. The hatched regions in all panels indicate significant ($p < 0.05$) trends. Note that the vertical axis is cropped below 1,000 m depths for panels e,f.

are related to another ocean bias: a too strong stratification in the Southern Ocean. The strong stratification prevents (deep) vertical mixing of relatively saline water towards the surface (van Westen and Dijkstra, 2020). The melting of sea ice and

245 snow (on top of the sea ice) under climate change contribute to the freshening of the Weddell Gyre in the absence of (deep) vertical mixing in the LR-CESM. The Southern Ocean stratification and (deep) vertical mixing are much better resolved in a high-resolution model (van Westen and Dijkstra, 2020) and explain the different salinity trends near the Weddell Gyre between the HR-CESM and LR-CESM. The salinity responses (at 34°S) below 1,000 m are much smaller and less zonally coherent compared to the upper 1,000 m. The climate change response is delayed at greater depth (by about 100 years), which explains

250 the differences in salinity trends between the upper 1,000 m and those below 1,000 m depth. Salinity changes in the deep water formation regions in the North Atlantic have only a limited effect within this 100-year period (model years 2000 – 2100).

For the HR-CESM, the ASW and AAIW are the main contributors (53.9% and 29.5%, respectively) to the F_{ovS} trend under climate change (Figure 2). The more saline ASW and AAIW water masses are the dominant factor in the F_{ovS} response. The lower zonally-averaged meridional velocities as a consequence of AMOC weakening slightly reduce the magnitude of

255 the ASW and AAIW trends. For the LR-CESM, the ASW, AAIW and NADW contribute 23.7%, 51.3%, 35.4% to the F_{ovS} trend, respectively (note that the AABW contributes -10.4%). The lower meridional velocities induce the negative ASW and AAIW freshwater responses, as these water masses become fresher over time. The negative NADW contribution is related to a freshening of this water mass and this freshening is partly related to changes in the vertical extent of the NADW (it extends into the relatively fresh AAIW over time). The AAIW, NADW and AABW contributions to the F_{ovS} trend are 58.6%, 20.6%,

260 -2.9% when fixing the vertical NADW extent to 1,000 – 4,000 m, respectively, the ASW contribution remains unaltered. This effect of the varying NADW extent is smaller in the HR-CESM (12.8% for varying and 7.4% for fixed NADW). Although the F_{ovS} decreases in both the HR-CESM and LR-CESM, the F_{ovS} responses is due to different processes, where it is mainly salinity dominated in the HR-CESM and overturning dominated in the LR-CESM.

3.4 CMIP6 Model Results

265 The systematic comparison between the HR-CESM and LR-CESM results clearly show the differences in the F_{ovS} values and the associated water masses, which are mainly related to the horizontal resolutions between the model configurations. To investigate whether these biases occur also in other models, we include an analysis of F_{ovS} using 39 different CMIP6 models (under the Hist/SSP5-8.5 scenario). Details about the CMIP6 models used are provided in Table A1.

In Figure 8 we present the F_{ovS} (components) and AMOC strength for the 39 CMIP6 models, together with the HR-CESM,

270 LR-CESM and reanalysis. First we compare all the models against the present-day (1994 – 2020) reanalysis (left column in Figure 8). We categorise the models in four different categories: models with a realistic present-day F_{ovS} (diamond markers, 13 CMIP6 models), models with a realistic present-day AMOC strength (circled markers, 7 CMIP6 models), models with both a realistic present-day F_{ovS} and AMOC strength (hexagon markers, 0 CMIP6 models) and the remaining models (crossed markers, 19 CMIP6 models). None of the CMIP6 models (and the HR-CESM and LR-CESM) have both a realistic present-day

275 F_{ovS} and realistic AMOC strength, and only reanalysis falls within this category. The 26 CMIP6 models with a positive F_{ovS} bias compared to observations have a stronger AMOC strength compared to the 13 models with a realistic F_{ovS} (mean AMOC

strength of 17.4 Sv and 12.6 Sv, respectively). Similar to the HR-CESM and LR-CESM, most of the F_{ovS} bias can be explained by the ASW and NADW contributions (Figures 8c,g).

For the 13 CMIP6 models with a realistic F_{ovS}, only four of them (CNRM-CM6-1, CNRM-ESM2-1, MCM-UA-1-0 and MRI-ESM2-0) have a reasonable present-day AMOC strength (≈ 15.5 Sv), but the remaining ones have a fairly weak AMOC strength (< 13.3 Sv). The CNRM-CM6-1, CNRM-ESM2-1 and MRI-ESM2-0 are relatively fresh (w.r.t. reanalysis) near 10°W and the surface, which results in a positive freshwater bias for the ASW but this is compensated by a smaller AAIW contribution. This relatively fresh bias appears (to some extent) in most of the CMIP6 models (Figure A1) and also in the HR-CESM and LR-CESM (Figure 5). The displayed CMIP6 profiles in Figure A1 are somewhat small and should only be used for pattern comparison. The freshwater bias near the surface is smaller in the MCM-UA-1-0 and is the one model closest to reanalysis for the AAIW freshwater contribution (Figure 8e). However, for the MCM-UA-1-0 the positive ASW freshwater bias is compensated by a stronger NADW freshwater export out of the Atlantic Ocean. It is interesting that the MCM-UA-1-0 is relatively close to reanalysis, given that this model has the lowest ocean resolution among the analysed models (Table A1). There are 7 CMIP6 models with a strong positive freshwater bias ($F_{\mathrm{ovS}} > 0.2$ Sv) and these models (e.g., FGOALS-f3-L, GISS-E2-2-G, TaiESM1) have an unrealistic mean state at 34°S. There is only one model (MCM-UA-1-0) which is close to reanalysis for the AAIW contribution (Figures 8e), and most models underestimate the AAIW contribution.

The MCM-UA-1-0 appears to be the model closest to observations and reanalysis, but this qualification changes when determining the present-day salinity and zonally-averaged meridional velocity root-mean-square errors (RMSEs) w.r.t. reanalysis at 34°S (inset in Figure 8h). The MCM-UA-1-0 has the second largest salinity RMSE and second largest velocity RMSE of all the diamond-labelled models (i.e., realistic F_{ovS}). The diamond-labelled models have on average the smallest salinity biases (relatively low salinity RMSE) of the CMIP6 suite, but regarding the velocity RMSE they are not considerably better than the other CMIP6 models because the diamond-labelled models have a relatively weak AMOC. The FGOALS-g3 has the lowest velocity RMSE, but this model has an unrealistic salinity profile and relatively strong AMOC strength (23.3 Sv) when comparing to reanalysis. These results underline that having a realistic F_{ovS} does not imply a realistic present-day mean state.

Similar to the CESM results, we find decreasing values in F_{ovS} (and its components) and AMOC strength under climate change (Figures 8b,d,f,h). The 13 CMIP6 models with a realistic present-day F_{ovS} show a much smaller F_{ovS} trend (-0.022 Sv per century) than in the remaining 26 CMIP6 models (-0.15 Sv per century). The ASW response is the dominant contributor in the F_{ovS} trend. Note that these F_{ovS} trends can either be salinity driven (as in the HR-CESM) or overturning driven (as in the LR-CESM).

The HR-CESM and LR-CESM results are consistent with the CMIP6 results and the CESM simulations are actually close to the CMIP6 mean (Figures 8). Most CMIP6 models and the CESM simulations are too fresh near the surface at 34°S (i.e., the ASW contribution), resulting in a positive freshwater F_{ovS} bias compared to observations. Models with a realistic F_{ovS} have either biases in the AAIW contribution, NADW contribution or AMOC strength. None of the models analysed here has a realistic present-day mean state when compared to available observations and reanalysis.
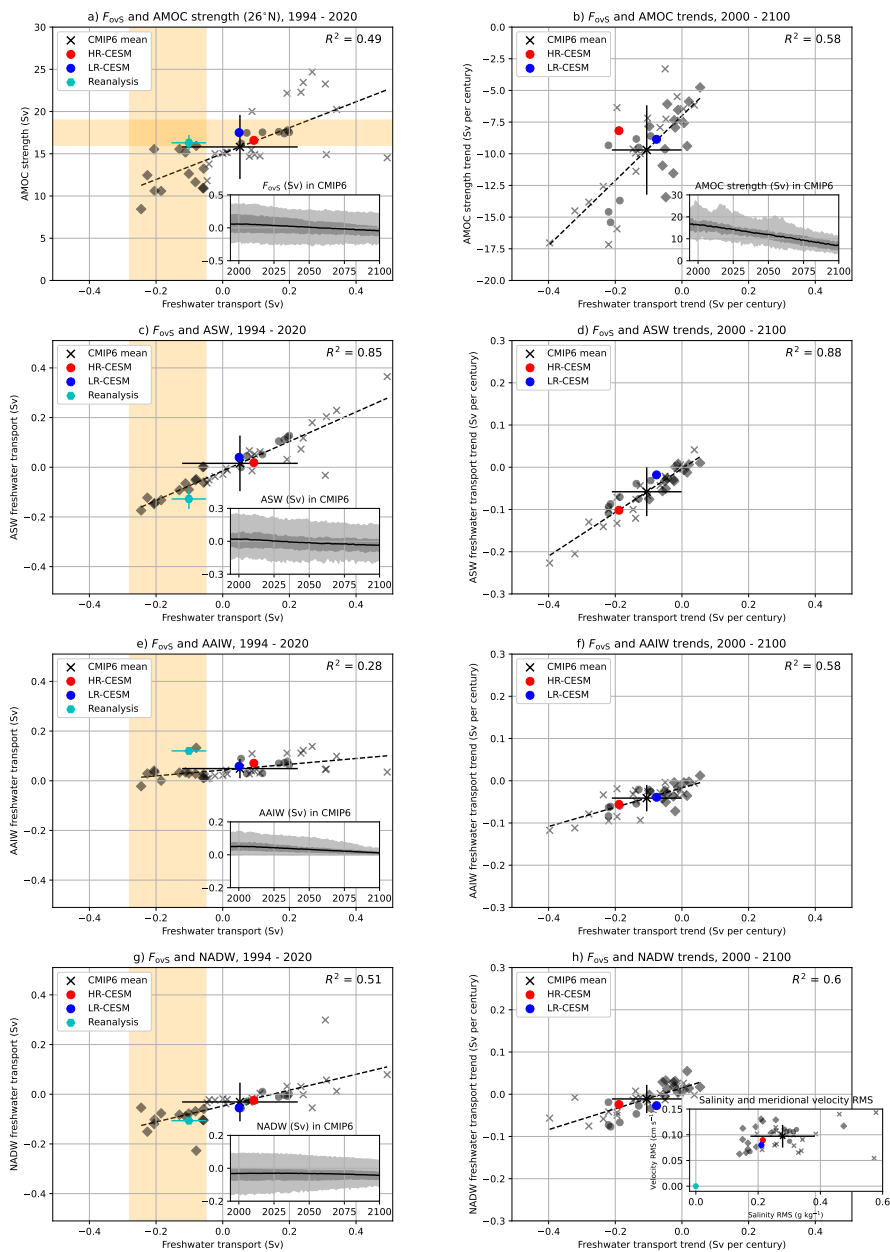
Figure 8. Left column: The present-day (model years 1994 – 2020) freshwater transport by AMOC (at 34°S, F_{ovS}) and a) AMOC strength (at 26°N and 1,000 m), c) ASW freshwater transport contribution, e) AAIW freshwater transport contribution and g) NADW freshwater transport contribution for CMIP6, HR-CESM, LR-CESM and reanalysis. The individual CMIP6 models are indicated in grey. The diamond and circle markers have a realistic (i.e., within a yellow band) F_{ovS} and AMOC strength, respectively, whereas the cross markers fall outside the yellow bands. Hexagon markers have both a realistic F_{ovS} and AMOC strength. Right column: Similar to a), c) and e), g), but now the trends (model years 2000 – 2100) in the freshwater transport (components) and AMOC strength. The insets in a), b), c), e), g) show the CMIP6 model mean (black line) and CMIP6 model variance (50% and 95%-confidence levels, shading) for the freshwater transports and AMOC strength over time. The inset in h) shows the model deviations w.r.t. reanalysis for the present-day salinity section and zonally-averaged (baroclinic) meridional velocity profile (at 34°S), here expressed as the weighted root-mean-square errors. The CMIP6 model mean and model standard deviation are also indicated in all panels. The dashed lines in all panels indicate the CMIP6 model regression, the R^2 value is indicated in the top right corner.

4 Summary and Discussion

Our analysis of CMIP6 models and high-resolution (HR) and low-resolution (LR) versions of the CESM has shown that persistent biases in these models remain in the AMOC induced Atlantic freshwater transport, as measured by F_{ovS}. The values of F_{ovS} from the reanalysis product (which is steered towards observations) is in good agreement with those from direct observations (Bryden et al., 2011; Garzoli et al., 2013). In the climate model simulations, numerous processes contribute to this deficiency in F_{ovS}: ITCZ positioning and strength, Agulhas Leakage, Indonesian Throughflow, AMOC strength, and ventilation of the AAIW and NADW. Biases in the ASW induce the most dominant F_{ovS} biases and occur on relative short time scales (years). Biases in the NADW also induce F_{ovS} biases but occur on longer (decadal-to-centennial) time scales.

Several model studies (Small et al., 2014; Jüling et al., 2021; van Westen et al., 2020; van Westen and Dijkstra, 2021) demonstrated oceanic bias reductions when increasing the horizontal resolution in the ocean model. However, here the F_{ovS} bias is larger in the HR-CESM PI control than the LR-CESM PI control (after model year 150). This larger bias is related to a faster (oceanic) adjustment in the higher horizontal resolution model which allows for more eddy-induced horizontal mixing ventilation. The freshwater convergence/divergence (ΔF_{ov}) is, however, fairly similar in HR-CESM and LR-CESM, which is related to a relatively large contribution of F_{ovN} in the LR-CESM. The ASW freshwater transport is fairly similar between the HR-CESM and LR-CESM PI control, but this contribution is mainly related to Indian Ocean's surface (0 – 100 m) salinity and is influenced by precipitation and the Indonesian Throughflow. These results suggest that increasing the ocean model horizontal resolution would have a limited impact on F_{ovS} biases as these biases are strongly controlled by those in the atmospheric model component.

To further explore the influence of atmospheric freshwater biases on F_{ovS}, we have conducted simulations with only the ocean component of the CESM (i.e., the Parallel Ocean Program, POP) with the prescribed Coordinated Ocean Reference Experiment (CORE, derived from observations) forcing dataset (Large and Yeager, 2004; Weijer et al., 2012; Le Bars et al., 2016). The surface (0 – 100 m) salinity biases substantially reduce in the Indian Ocean in the stand-alone POP simulation (0.1° horizontal resolution) and hence reduce the ASW biases (Figure 9). The NADW in the stand-alone POP remains close to reanalysis after 250 years of model integration, whereas the NADW in the HR-CESM PI control simulation has strongly drifted over this period (Figure 2e). This indicates that the atmospheric component and fluxes need to be improved in the coupled climate simulations to have a realistic salinity distribution, specifically in the Indian Ocean. Once in coupled interaction with the other model components, this would likely then reduce the biases in the Atlantic Surface Water component of F_{ovS}.

The biases in F_{ovS} due to atmospheric biases is found not only in CESM, but in a large number of CMIP6 models. The CMIP6 model mean has a positive F_{ovS} bias which is similar as in the CMIP5 results (Mecking et al., 2017). Values of F_{ovS} decrease under climate change in both versions of the CESM, but the changes are salinity driven in the HR-CESM while for the LR-CESM the changes are overturning driven. Most of the CMIP6 models have similar biases as in the CESM. The models with a realistic F_{ovS} have biases elsewhere, for example their F_{ovS} contributions of the AAIW and their AMOC strengths are underestimated. The bottom line is that CMIP6 models either have a too weak present-day AMOC or have a wrong sign of F_{ovS}.
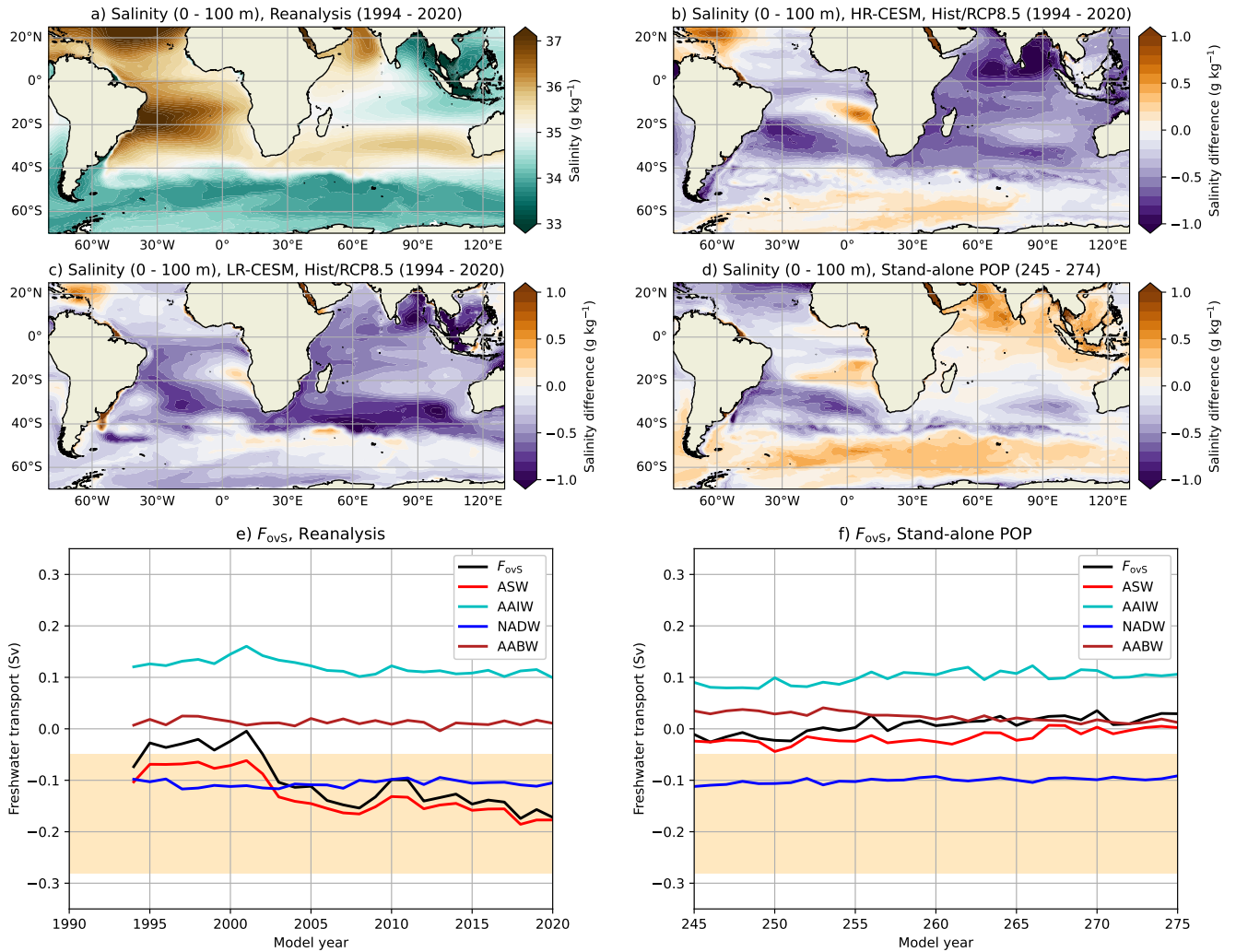
Figure 9. (a – d): The present-day (1994 – 2020) and vertically-averaged (0 – 100 m) salinity for a) Reanalysis, b) HR-CESM and c) LR-CESM. For the d) stand-alone POP the time mean of model years 245 – 274 is shown. For the HR-CESM, LR-CESM and stand-alone POP, the salinity differences compared to reanalysis are displayed, where the reanalysis data is re-gridded onto each model grid. (e & f): The freshwater transport at $34°$S and its components for e) Reanalysis and the f) stand-alone POP, the time series for the HR-CESM and LR-CESM are already shown in Figure 2.

In state-of-the-art climate models, such as in the latest CMIP6 models, the AMOC weakens under future climate change (Weijer et al., 2020; van Westen et al., 2020) but no (abrupt) AMOC collapses are found. However, it is questionable whether these climate models are fit for purpose to determine the risk of AMOC tipping, because of their biases identified here and mainly the wrong sign of F_{ovS}. The absence of AMOC tipping can be connected to the results from idealised climate models (Dijkstra, 2007; Huisman et al., 2010), which suggest that the AMOC is in its monostable (bistable) regime when F_{ovS} is positive (negative). However, there has been substantial criticism on this aspect of F_{ovS} (Gent, 2018; Mignac et al., 2019; Haines et al., 2022). For example, Haines et al. (2022) show that in 10 CMIP5 models the variations in F_{ovS} do not influence the AMOC strength. However, the AMOC strength in these models poorly matches with that from observations, likely related to a coarse ($> 1°$) horizontal ocean resolution. The AMOC in EC-Earth3 and MPI-ESM1-2-HR does not show transition behaviour (Jackson et al., 2022) under the chosen forcing scenario while having a slightly negative F_{ovS} (Table A1). These two CMIP6 models also have a relatively weak AMOC strength (< 14 Sv), a too fresh ASW and a too saline NADW. These biases likely influence the salt-advection feedback strength and hence the AMOC responses. In Gent (2018) it is stated that the wind-driven salinity transport is not taken into account properly when the AMOC strength varies. However, as argued in Weijer et al. (2019), the wind-driven transport is ineffective in changing the salinity in the Atlantic as a whole and hence does not control the stability of the AMOC. Atmospheric feedbacks, such as the shift of the ITCZ due to AMOC, are not accounted for in F_{ovS}, but the available model studies (Den Toom et al., 2012; Castellana and Dijkstra, 2020) have indicated that these effects are small. While this issue is far from settled, if $F_{ovS} < 0$ is indeed an indicator for the existence of a multi-stable AMOC regime then models with $F_{ovS} > 0$ grossly underestimate the probability that an AMOC collapse can occur.

The results presented in this study show persistent freshwater transport biases in the latest state-of-the-art climate models. The resulting effect of these biases is that the major salt-advection feedback is not adequately represented. This leads to an underestimation of AMOC weakening under climate change and freshwater forcing experiments and likely reduces the probability of AMOC tipping. Because such AMOC weakening and/or tipping can disrupt society worldwide within a few decades, it is very urgent that the model biases are being reduced so that proper estimates of tipping probabilities can be obtained.

Code and data availability. Model output for the CESM simulations can accessed at https://ihesp.github.io/archive/. The processed model output and analysis scripts can be accessed at https://doi.org/10.5281/zenodo.10684732, including additional (i.e., not shown) material. The reanalysis product is available at https://doi.org/10.48670/moi-00021. The CMIP6 model output is provided by the World Climate Research Programme's Working Group on Coupled Modeling.

Author contributions. R.M.v.W. and H.A.D. conceived the idea for this study. R.M.v.W. conducted the analysis and prepared all figures. Both authors were actively involved in the interpretation of the analysis results and the writing process.
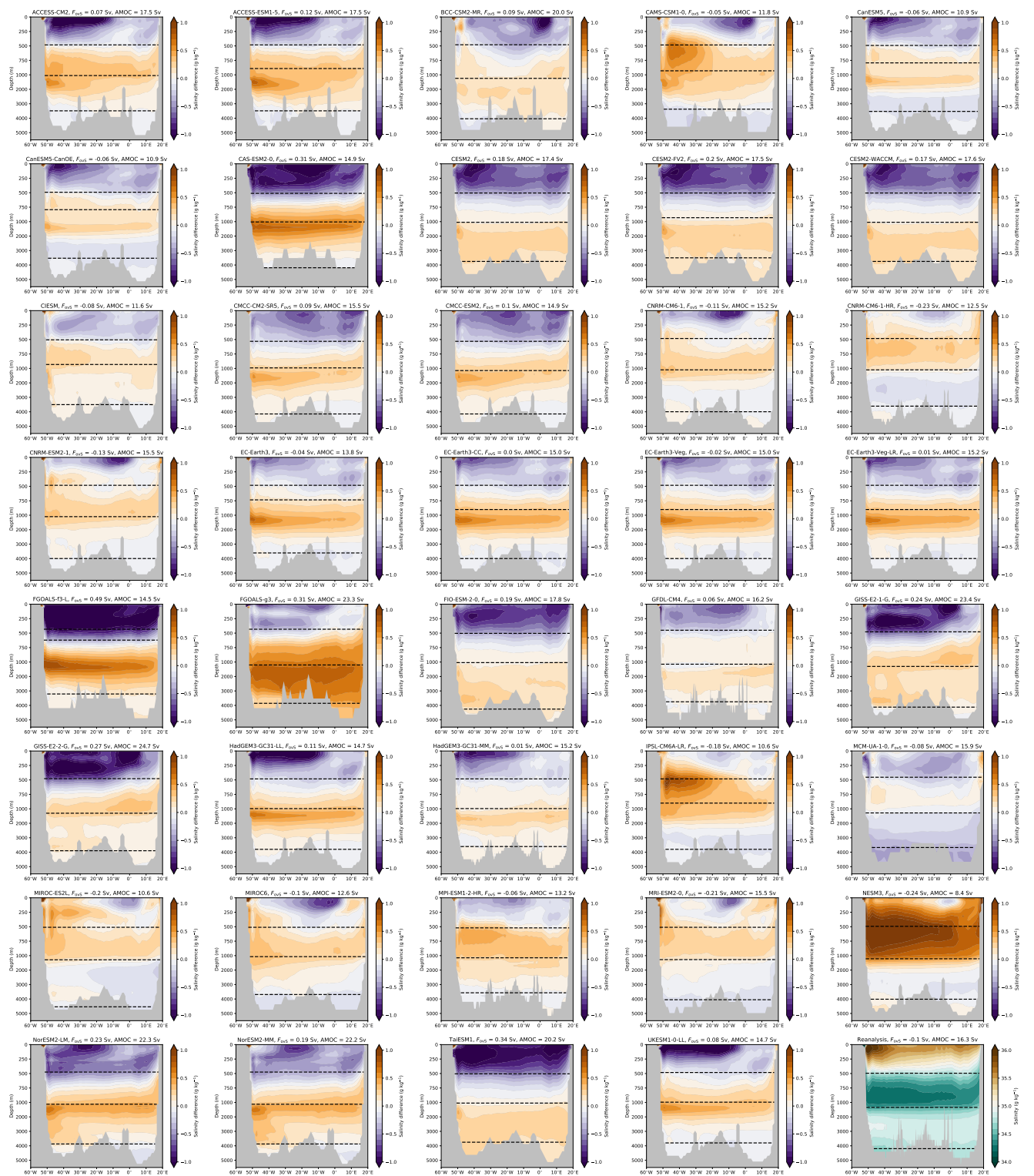
Figure A1. The present-day (1994 – 2020) salinity at 34°S for the 39 CMIP6 models and reanalysis (lower right). For CMIP6, the salinity differences compared to reanalysis are displayed, the reanalysis data is regridded onto each CMIP model grid. The present-day (1994 – 2020) F_{ovS} and AMOC strength (1,000 m and 26°N) are displayed at the top of each panel. The dashed lines indicate the different water masses (top to bottom: ASW, AAIW, NADW and AABW). Note that the vertical axis is cropped below 1,000 m depths.

Competing interests. The authors declare no competing interests.

375 *Acknowledgements.* The analysis of all the model output was conducted on the Dutch National Supercomputer Snellius. R.M.v.W. and H.A.D. are funded by the European Research Council through the ERC-AdG project TAOC (project 101055096)

References

Armstrong McKay, D. I., Staal, A., Abrams, J. F., Winkelmann, R., Sakschewski, B., Loriani, S., Fetzer, I., Cornell, S. E., Rockström, J., and Lenton, T. M.: Exceeding 1.5 C global warming could trigger multiple climate tipping points, Science, 377, eabn7950, 2022.

Bryden, H. L., King, B. A., and McCarthy, G. D.: South Atlantic overturning circulation at 24 S, Journal of Marine Research, 69, 38–55, 2011.

Caesar, L., Rahmstorf, S., Robinson, A., Feulner, G., and Saba, V.: Observed fingerprint of a weakening Atlantic Ocean overturning circulation, Nature, 556, 191–196, 2018.

Caesar, L., McCarthy, G. D., Thornalley, D., Cahill, N., and Rahmstorf, S.: Current Atlantic meridional overturning circulation weakest in last millennium, Nature Geoscience, 14, 118–120, 2021.

Castellana, D. and Dijkstra, H. A.: Noise-induced transitions of the Atlantic Meridional Overturning Circulation in CMIP5 models, Scientific Reports, 10, 1–9, 2020.

Castellana, D., Baars, S., Wubs, F. W., and Dijkstra, H. A.: Transition probabilities of noise-induced transitions of the Atlantic Ocean circulation, Scientific Reports, 9, 20 284, 2019.

Chang, P., Zhang, S., Danabasoglu, G., Yeager, S. G., Fu, H., Wang, H., Castruccio, F. S., Chen, Y., Edwards, J., Fu, D., et al.: An unprecedented set of high-resolution earth system simulations for understanding multiscale interactions in climate variability and change, Journal of Advances in Modeling Earth Systems, 12, e2020MS002 298, 2020.

de Vries, P. and Weber, S. L.: The Atlantic freshwater budget as a diagnostic for the existence of a stable shut down of the meridional overturning circulation, Geophysical Research Letters, 32, 2005.

Den Toom, M., Dijkstra, H. A., Cimatoribus, A. A., and Drijfhout, S. S.: Effect of atmospheric feedbacks on the stability of the Atlantic meridional overturning circulation, Journal of climate, 25, 4081–4096, 2012.

Dijkstra, H. A.: Characterization of the multiple equilibria regime in a global ocean model, Tellus, 59A, 695–705, 2007.

Drijfhout, S. S., Weber, S. L., and van der Swaluw, E.: The stability of the MOC as diagnosed from model projections for pre-industrial, present and future climates, Climate Dynamics, 37, 1575–1586, https://doi.org/10.1007/s00382-010-0930-z, 2011.

Garzoli, S. L., Baringer, M. O., Dong, S., Perez, R. C., and Yao, Q.: South Atlantic meridional fluxes, Deep Sea Research Part I: Oceanographic Research Papers, 71, 21–32, 2013.

Gent, P. R.: A commentary on the Atlantic meridional overturning circulation stability in climate models, Ocean Modelling, 122, 57–66, 2018.

Haines, K., Ferreira, D., and Mignac, D.: Variability and Feedbacks in the Atlantic Freshwater Budget of CMIP5 Models With Reference to Atlantic Meridional Overturning Circulation Stability, Front. Mar. Sci, 9, 2022.

Huisman, S. E., Den Toom, M., Dijkstra, H. A., and Drijfhout, S.: An indicator of the multiple equilibria regime of the Atlantic meridional overturning circulation, Journal of Physical Oceanography, 40, 551–567, 2010.

Jackson, L.: Shutdown and recovery of the AMOC in a coupled global climate model: the role of the advective feedback, Geophysical Research Letters, 40, 1182–1188, 2013.

Jackson, L. C., Alastrué de Asenjo, E., Bellomo, K., Danabasoglu, G., Haak, H., Hu, A., Jungclaus, J., Lee, W., Meccia, V. L., Saenko, O., et al.: Understanding AMOC stability: the North Atlantic hosing model intercomparison project, Geoscientific Model Development Discussions, 2022, 1–32, 2022.

Johns, W. E., Baringer, M. O., Beal, L., Cunningham, S., Kanzow, T., Bryden, H. L., Hirschi, J., Marotzke, J., Meinen, C., Shaw, B., et al.: Continuous, array-based estimates of Atlantic Ocean heat transport at 26.5 N, Journal of Climate, 24, 2429–2449, 2011.

415 Jüling, A., Zhang, X., Castellana, D., Von Der Heydt, A. S., and Dijkstra, H. A.: The Atlantic's freshwater budget under climate change in the Community Earth System Model with strongly eddying oceans, Ocean Science, 17, 729–754, 2021.

Large, W. G. and Yeager, S. G.: Diurnal to decadal global forcing for ocean and sea-ice models: The data sets and flux climatologies, 2004.

Le Bars, D., Viebahn, J., and Dijkstra, H.: A Southern Ocean mode of multidecadal variability, Geophysical Research Letters, 43, 2102–2110, 2016.

420 Liu, H. and Wang, S.: Approximation of Stochastic Invariant Manifolds, 2014.

Liu, W., Xie, S.-P., Liu, Z., and Zhu, J.: Overlooked possibility of a collapsed Atlantic Meridional Overturning Circulation in warming climate, Science Advances, 3, e1601 666, https://doi.org/10.1126/sciadv.1601666, 2017.

Lobelle, D., Beaulieu, C., Livina, V., Sevellec, F., and Frajka-Williams, E.: Detectability of an AMOC decline in current and projected climate changes, Geophysical Research Letters, 47, e2020GL089 974, 2020.

425 Mamalakis, A., Randerson, J. T., Yu, J.-Y., Pritchard, M. S., Magnusdottir, G., Smyth, P., Levine, P. A., Yu, S., and Foufoula-Georgiou, E.: Zonally contrasting shifts of the tropical rain belt in response to climate change, Nature Climate Change, 11, 143–151, 2021.

Marotzke, J.: Abrupt climate change and thermohaline circulation: Mechanisms and Predictability, Proc. Natl. Acad. Sci., 97, 1347–1350, 2000.

McFarlane, A. A. and Frierson, D. M.: The role of ocean fluxes and radiative forcings in determining tropical rainfall shifts in RCP8.5 430 simulations, Geophysical Research Letters, 44, 8656–8664, 2017.

Mecking, J., Drijfhout, S. S., Jackson, L. C., and Graham, T.: Stable AMOC off state in an eddy-permitting coupled climate model, Climate Dynamics, 47, 2455–2470, 2016.

Mecking, J., Drijfhout, S., Jackson, L., and Andrews, M.: The effect of model bias on Atlantic freshwater transport and implications for AMOC bi-stability, Tellus A: Dynamic Meteorology and Oceanography, 69, 1299 910, 2017.

435 Mecking, J. V. and Drijfhout, S. S.: The decrease in ocean heat transport in response to global warming, Nature Climate Change, 13, 1229–1236, 2023.

Menary, M. B., Robson, J., Allan, R. P., Booth, B. B., Cassou, C., Gastineau, G., Gregory, J., Hodson, D., Jones, C., Mignot, J., et al.: Aerosol-forced AMOC changes in CMIP6 historical simulations, Geophysical Research Letters, 47, e2020GL088 166, 2020.

Mignac, D., Ferreira, D., and Haines, K.: Decoupled freshwater transport and meridional overturning in the South Atlantic, Geophysical 440 Research Letters, 46, 2178–2186, 2019.

Orihuela-Pinto, B., England, M. H., and Taschetto, A. S.: Interbasin and interhemispheric impacts of a collapsed Atlantic Overturning Circulation, Nature Climate Change, 12, 558–565, 2022.

Peltier, W. R. and Vettoretti, G.: Dansgaard-Oeschger oscillations predicted in a comprehensive model of glacial climate: A "kicked" salt oscillator in the Atlantic, Geophysical Research Letters, 41, 7306–7313, 2014.

445 Rahmstorf, S.: On the freshwater forcing and transport of the Atlantic thermohaline circulation, Climate Dynamics, 12, 799–811, https://doi.org/10.1007/s003820050144, 1996.

Rahmstorf, S., Crucifix, M., Ganopolski, A., Goosse, H., Kamenkovich, I., Knutti, R., Lohmann, G., March, R., Mysak, L., Wang, Z., and Weaver, A. J.: Thermohaline circulation hysteresis: a model intercomparison, Geophysical Research Letters, L23605, 1–5, 2005.

Rousselet, L., Cessi, P., and Forget, G.: Coupling of the mid-depth and abyssal components of the global overturning circulation according 450 to a state estimate, Science Advances, 7, eabf5478, 2021.

Santer, B. D., Wigley, T., Boyle, J., Gaffen, D. J., Hnilo, J., Nychka, D., Parker, D., and Taylor, K.: Statistical significance of trends and trend differences in layer-average atmospheric temperature time series, Journal of Geophysical Research: Atmospheres, 105, 7337–7356, 2000.

Small, R. J., Bacmeister, J., Bailey, D., Baker, A., Bishop, S., Bryan, F., Caron, J., Dennis, J., Gent, P., Hsu, H.-m., et al.: A new synoptic scale resolving global climate simulation using the Community Earth System Model, Journal of Advances in Modeling Earth Systems, 6, 1065–1094, 2014.

Smeed, D. A., Josey, S., Beaulieu, C., Johns, W., Moat, B. I., Frajka-Williams, E., Rayner, D., Meinen, C. S., Baringer, M. O., Bryden, H. L., et al.: The North Atlantic Ocean is in a state of reduced overturning, Geophysical Research Letters, 45, 1527–1533, 2018.

Stommel, H.: Thermohaline convection with two stable regimes of flow, Tellus, 13, 224–230, 1961.

van Westen, R. M. and Dijkstra, H. A.: Multidecadal preconditioning of the Maud Rise polynya region, Ocean Science, 16, 1443–1457, 2020.

van Westen, R. M. and Dijkstra, H. A.: Ocean eddies strongly affect global mean sea-level projections, Science advances, 7, eabf1674, 2021.

van Westen, R. M., Dijkstra, H. A., van der Boog, C. G., Katsman, C. A., James, R. K., Bouma, T. J., Kleptsova, O., Klees, R., Riva, R. E., Slobbe, D. C., et al.: Ocean model resolution dependence of Caribbean sea-level projections, Scientific reports, 10, 14 599, 2020.

van Westen, R. M., Dijkstra, H. A., and Bloemendaal, N.: Mechanisms of tropical cyclone response under climate change in the community earth system model, Climate Dynamics, pp. 1–16, 2023.

Weijer, W., Maltrud, M., Hecht, M., Dijkstra, H., and Kliphuis, M.: Response of the Atlantic Ocean circulation to Greenland Ice Sheet melting in a strongly-eddying ocean model, Geophysical Research Letters, 39, 2012.

Weijer, W., Cheng, W., Drijfhout, S. S., Fedorov, A. V., Hu, A., Jackson, L. C., Liu, W., McDonagh, E., Mecking, J., and Zhang, J.: Stability of the Atlantic Meridional Overturning Circulation: A review and synthesis, Journal of Geophysical Research: Oceans, 124, 5336–5375, 2019.

Weijer, W., Cheng, W., Garuba, O. A., Hu, A., and Nadiga, B. T.: CMIP6 Models Predict Significant 21st Century Decline of the Atlantic Meridional Overturning Circulation, Geophysical Research Letters, 47, e2019GL08 607, https://doi.org/10.1029/2019gl086075, 2020.

Worthington, E. L., Moat, B. I., Smeed, D. A., Mecking, J. V., Marsh, R., and McCarthy, G. D.: A 30-year reconstruction of the Atlantic meridional overturning circulation shows no decline, Ocean Science, 17, 285–299, 2021.

Yin, J. and Stouffer, R. J.: Comparison of the stability of the Atlantic thermohaline circulation in two coupled atmosphere - Ocean general circulation models, Journal of Climate, 20, 4293–4315, https://doi.org/10.1175/JCLI4256.1, 2007.

Table A1. The models used in this study with the dimensions of the ocean component, the AMOC strength and the F_{ovS} (contributions) for the present-day period (1994 – 2020).

Model name	Number of dimensions (lon × lat × depth)	AMOC (Sv)	F_{ovS} (Sv)	ASW (Sv)	AAIW (Sv)	NADW (Sv)	AABW (Sv)
Reanalysis	4320 × 2041 × 50	16.3	-0.10	-0.13	0.12	-0.11	0.01
HR-CESM	3600 × 2400 × 62	16.6	0.09	0.02	0.07	-0.02	0.03
LR-CESM	320 × 384 × 60	17.5	0.05	0.04	0.06	-0.05	0.01
ACCESS-CM2	360 × 300 × 50	17.5	0.07	0.05	0.03	-0.03	0.03
ACCESS-ESM1-5	360 × 300 × 50	17.5	0.12	0.05	0.03	0.01	0.03
BCC-CSM2-MR	360 × 232 × 40	20.0	0.09	-0.01	0.11	-0.02	0.01
CAMS-CSM1-0	360 × 200 × 50	11.8	-0.05	-0.06	0.01	-0.03	0.04
CanESM5	360 × 291 × 45	10.9	-0.06	0.0	0.01	-0.1	0.03
CanESM5-CanOE	360 × 291 × 45	10.9	-0.06	0.0	0.01	-0.1	0.03
CAS-ESM2-0	360 × 196 × 30	14.9	0.31	0.2	0.05	0.06	0.0
CESM2	320 × 384 × 60	17.4	0.18	0.11	0.07	-0.0	0.0
CESM2-FV2	320 × 384 × 60	17.5	0.2	0.13	0.06	0.0	0.01
CESM2-WACCM	320 × 384 × 60	17.6	0.17	0.11	0.07	-0.01	0.0
CIESM	320 × 384 × 60	11.6	-0.08	-0.05	0.03	-0.07	0.01
CMCC-CM2-SR5	362 × 292 × 50	15.5	0.09	0.04	0.04	-0.03	0.03
CMCC-ESM2	362 × 292 × 50	14.9	0.1	0.05	0.04	-0.03	0.03
CNRM-CM6-1	362 × 294 × 75	15.2	-0.11	-0.07	0.03	-0.09	0.01
CNRM-CM6-1-HR	1442 × 1050 × 75	12.5	-0.23	-0.12	0.03	-0.15	0.02
CNRM-ESM2-1	362 × 294 × 75	15.5	-0.13	-0.09	0.03	-0.08	0.01
EC-Earth3	362 × 292 × 75	13.8	-0.04	-0.05	0.01	-0.02	0.02
EC-Earth3-CC	362 × 292 × 75	15.0	0.0	-0.03	0.02	-0.02	0.03
EC-Earth3-Veg	362 × 292 × 75	15.0	-0.02	-0.04	0.02	-0.02	0.02
EC-Earth3-Veg-LR	362 × 292 × 75	15.2	0.01	-0.01	0.03	-0.02	0.02
FGOALS-f3-L	360 × 218 × 30	14.5	0.49	0.36	0.03	0.08	0.01
FGOALS-g3	360 × 218 × 30	23.3	0.31	-0.03	0.05	0.3	-0.0
FIO-ESM-2-0	320 × 384 × 60	17.8	0.19	0.12	0.08	-0.01	0.0
GFDL-CM4	1440 × 1080 × 35	16.2	0.06	-0.0	0.09	-0.06	0.02
GISS-E2-1-G	288 × 180 × 40	23.4	0.24	0.12	0.12	-0.0	0.0
GISS-E2-2-G	288 × 180 × 40	24.7	0.27	0.18	0.14	-0.05	0.01
HadGEM3-GC31-LL	360 × 330 × 75	14.7	0.11	0.06	0.03	0.0	0.01
HadGEM3-GC31-MM	1440 × 1205 × 75	15.2	0.01	-0.0	0.04	-0.04	0.01
IPSL-CM6A-LR	362 × 332 × 75	10.6	-0.18	-0.13	0.0	-0.08	0.02
MCM-UA-1-0	192 × 80 × 18	15.9	-0.08	-0.05	0.13	-0.23	0.06
MIROC-ES2L	360 × 256 × 63	10.6	-0.2	-0.14	0.03	-0.1	0.01
MIROC6	360 × 256 × 63	12.6	-0.1	-0.09	0.03	-0.08	0.04
MPI-ESM1-2-HR	802 × 404 × 40	13.2	-0.06	-0.06	0.03	-0.06	0.04
MRI-ESM2-0	360 × 363 × 61	15.5	-0.21	-0.15	0.04	-0.12	0.02
NESM3	362 × 292 × 46	8.4	-0.24	-0.17	-0.02	-0.05	0.01
NorESM2-LM	360 × 385 × 70	22.3	0.23	0.07	0.11	0.03	0.02
NorESM2-MM	360 × 385 × 70	22.2	0.19	0.03	0.11	0.03	0.02
TaiESM1	320 × 384 × 60	20.2	0.34	0.23	0.1	0.01	0.0
UKESM1-0-LL	360 × 330 × 75	14.7	0.08	0.07	0.03	-0.03	0.02